Journal of
Materials Chemistry A

PAPER

Check for updates

Enhanced thermoelectric performance in Fe$_2$V$_{0.8}$W$_{0.2}$Al thin films: synergistic effects of chemical ordering and tungsten substitution

Jose María Domínguez-Vázquez, [iD] [a] Miguel Ángel Tenaguillo, [iD] [a] Ketan Lohani, [iD] [a] Olga Caballero-Calero, [iD] [a] Cristina V. Manzano, [iD] [a] José J. Plata, [iD] [b] Antonio M. Marquez, [iD] [b] Alfonso Cebollada, [iD] [a] Andres Conca [iD] *[a] and Marisol Martín-González [iD] *[a]

We systematically investigate the combined effect of chemical ordering and W substitution on the thermoelectric properties of Fe$_2$V$_{0.8}$W$_{0.2}$Al thin films. Through controlled sputter deposition on MgO (100) and Al$_2$O$_3$ (11$\bar{2}$0) substrates at temperatures ranging from 350 °C to 950 °C, we achieve varying degrees of crystalline and chemical order. Films deposited between 750 °C and 950 °C adopt the highly ordered L2$_1$ phase, exhibiting a dramatic enhancement in Seebeck coefficient and substantial reduction in thermal conductivity compared to isostructural Fe$_2$VAl thin films without tungsten substitution. These synergistic improvements, attributed to electronic structure modifications and enhanced phonon scattering mechanisms, yield exceptional thermoelectric performance with maximum power factors of 730 ± 70 μW m^{-1} K^{-2} and figure of merit zT = 0.12 ± 0.03 at room temperature, representing a more than four-fold enhancement over undoped Fe$_2$VAl and demonstrating the potential for sustainable energy harvesting applications.

Introduction

Thermoelectric materials are the ones capable of converting thermal gradients into voltage differences. This characteristic makes them candidates for increasing global energy efficiency through waste-heat recovery. They also offer a solution for powering Internet of Things (IoT) and wearable devices through solid-state, noise-free means. The efficiency of a thermoelectric device is evaluated through the dimensionless figure of merit (zT), which is defined as $zT = S^2 \cdot \sigma \cdot T / \kappa$, where S, σ, T, and, κ, are respectively the Seebeck coefficient, the electrical conductivity, absolute temperature and the thermal conductivity of the studied material. Therefore, highly efficient thermoelectric materials must exhibit high Seebeck coefficient (S) and electrical conductivity (σ), which combine to form the power factor (PF = $S^2 \cdot \sigma$), while having low thermal conductivity (κ).[1]

Current state-of-the-art thermoelectric materials include bismuth telluride (Bi$_2$Te$_3$),[2,3] lead telluride (PbTe),[4] and metal selenides (Ag$_2$Se,[5,6,7] SnSe[8,9] and Cu$_2$Se[10,11]) for specific temperature windows. However, the practical implementation of these materials faces significant challenges including elemental scarcity, high-cost, and environmental toxicity concerns, which substantially limit their widespread technological deployment.

In recent years, half-Heusler (XYZ) and full-Heusler (X$_2$YZ) alloys have emerged as compelling alternatives, particularly those based on earth-abundant elements,[12] where X and Y are transition metals and Z is a p-block element. These materials offer the dual advantages of environmental sustainability and potentially lower manufacturing costs, while maintaining competitive thermoelectric performance.

Structurally, full Heusler alloys consist of three interpenetrating cubic lattices in which, ideally, each element is placed in a determined position. In this so-called L2$_1$ phase, superperiodicities appear along the [100] and [111] directions. However, the alloy can also present different degrees of chemical disorder. In this way, when the Y and Z elements exchange positions indistinctly, the superperiodicity along the [111] directions disappear. The resulting structure is called B2. Further, the alloy can present additional chemical disorder, the so-called A2 phase, where the positions of the three elements of the alloy exchange at random. In this case, the double periodicity along the [100] directions also disappear. Literature suggests[13,14] simultaneous appearance of these phases such as, *e.g.*, a mostly B2 ordered material with a small degree of A2 disorder, or a mostly L2$_1$ ordered system with a fraction of B2 phase are also possible. These three feasible structures for the specific material studied in this work are depicted in Fig. 1.

[a]Instituto de Micro y Nanotecnología, IMN-CNM, CSIC (CEI UAM+CSIC), Isaac Newton 8, Tres Cantos E-28760, Madrid, Spain. E-mail: andres.conca@csic.es; marisol. martin@csic.es

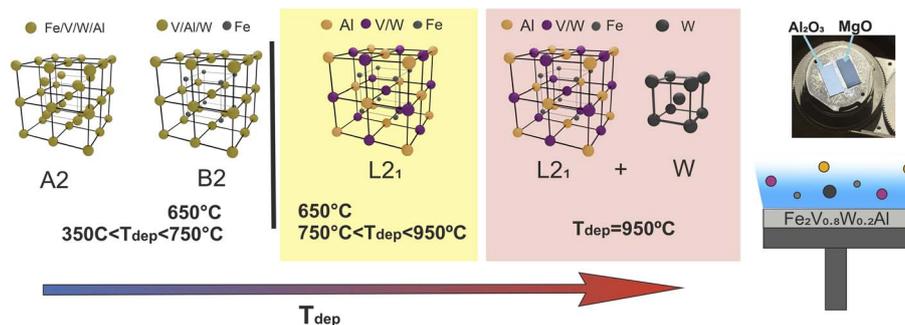*[b]Departamento de Química Física, Facultad de Química, Universidad de Sevilla, Seville, Spain*

This journal is © The Royal Society of Chemistry 2026

J. Mater. Chem. A, 2026, **14**, 12835–12845 | **12835**

Fig. 1 Left: the highest chemically ordered structure of $Fe_2V_{0.8}W_{0.2}Al$ obtained through magnetron sputtering at different deposition temperatures, ranging from 350 °C on MgO and Al_2O_3. Three main zones are distinguished: T_{dep} < 750 °C, where samples show B2 or A2 ordering. Between 750–950 °C (highlighted in yellow), where the $L2_1$ order is observed. Additionally, T_{dep} = 950 °C (highlighted in red), where apart from $L2_1$ ordering, W crystallization is observed. Right: image of the two types of substrates mounted in the sputtering holder for simultaneous deposition, along with a schematic of the different atoms ejected in the sputtering process off a $Fe_2V_{0.8}W_{0.2}Al$ target.

Among all Heusler alloys, Fe_2VAl-based full Heusler family stands out as one of the most interesting for thermoelectric applications. This narrow-gap alloy is constituted by non-toxic and abundant materials, while also exhibiting high power factors. In fact, the thermoelectric performance of this material can be greatly enhanced by growing Fe_2VAl thin films with the $L2_1$ chemically ordered structure, which fundamentally alters the electronic band structure and creates favorable conditions for enhanced Seebeck coefficients and reduced thermal conductivity, as we have shown in a previous work.[15]

Strategic elemental substitution enables precise control over carrier type and concentration, allowing optimization of thermoelectric properties. Environmentally benign dopants such as Ti^{16} $W^{17,18,19}$ $Ta^{20,21}$ or $Si^{22,23}$ offer particular advantages due to their non-toxicity and relative abundance. W is especially of great interest, for thermal conductivity reduction, the incorporation of heavy elements introduces additional phonon scattering centers, significantly suppressing the lattice thermal conductivity and consequently enhancing the overall figure of merit.[19,24]

Previous investigations have explored tungsten-doped Fe_2VAl systems with mixed results. For example, Machda et al.[17] and Hinterleitner et al.[18] studied W-doped thin films on silicon substrates, achieving zT values ranging from 0.15 to a remarkable value approaching 6. However, the interpretation of these findings is complicated by substrate interactions. Conversely, Mikami et al.[25] studied bulk tungsten-substituted materials, obtaining zT values in the 0.1–0.2 range. Despite these efforts, a systematic investigation correlating the effects of simultaneous chemical ordering and tungsten substitution in epitaxial thin films remain limited. This represents a significant knowledge gap in the understanding of the structure–property relationships for these films.

This work systematically explores the relationship between chemical ordering and tungsten substitution in $Fe_2V_{0.8}W_{0.2}Al$ thin films. We grew these films at various deposition temperatures on both MgO (100) and Al_2O_3 (11$\bar{2}$0) substrates to achieve different crystallographic orientations, specifically (100) and (110). This controlled approach allows us to disentangle the individual effects of substrate-mediated growth, crystalline

orientation, and chemical ordering on the material's properties. By gaining a fundamental understanding of these mechanisms, we can better explain the enhanced thermoelectric performance measured in our tungsten-substituted Heusler alloy films.

Results and discussion

Fig. 1 illustrates the experimental setup showing dual-substrate mounting configuration enabling simultaneous deposition on both MgO (100) and Al_2O_3 (11$\bar{2}$0) substrates on which the $Fe_2V_{0.8}W_{0.2}Al$ is sputtered from a single stoichiometric target. Systematic X-ray diffraction (XRD) analysis reveals distinct degree of chemical order as a function of the deposition temperature, with characteristic superstructure reflections serving as phase identification markers. The complete set of (XRD) measurements is shown in the SI.

For deposition temperature (T_{dep}) between 350 °C and 650 °C (750 °C for Al_2O_3 substrates), the chemically disordered A2 phase is obtained. An intermediate B2 phase emerges for films grown between 550 °C and 750 °C on MgO (100) substrates, as evidenced by (2 0 0) diffraction peak appearance. The highly ordered $L2_1$ structure develops for T_{dep} between 650 °C (750 °C for Al_2O_3 substrates) and 900 °C, confirmed by the emergence of characteristic (111) superstructure reflections.

At the highest deposition temperature T_{dep} = 950 °C, additional diffraction peaks corresponding to pure W phases appear alongside the $L2_1$ reflections on both substrates, indicating thermally-activated segregation of tungsten from the Heusler lattice. This segregation phenomenon is independent of substrate-induced strain effects and represents the upper temperature limit for the formation of $L2_1$ single-phase $Fe_2V_{0.8}W_{0.2}Al$.

Room temperature thermoelectric properties of all films as a function of deposition temperature are shown in Fig. 2, with background coloring distinguishing different phase regions: white (A2–B2 phases), yellow (pure $L2_1$ phase), and light red ($L2_1$ + tungsten segregation).

The Seebeck coefficient, electrical conductivity, and power factor of (100) and (110) oriented $Fe_2V_{0.8}W_{0.2}Al$ films are plotted versus the deposition temperature (T_{dep}), along with the

12836 | J. Mater. Chem. A, 2026, **14**, 12835–12845
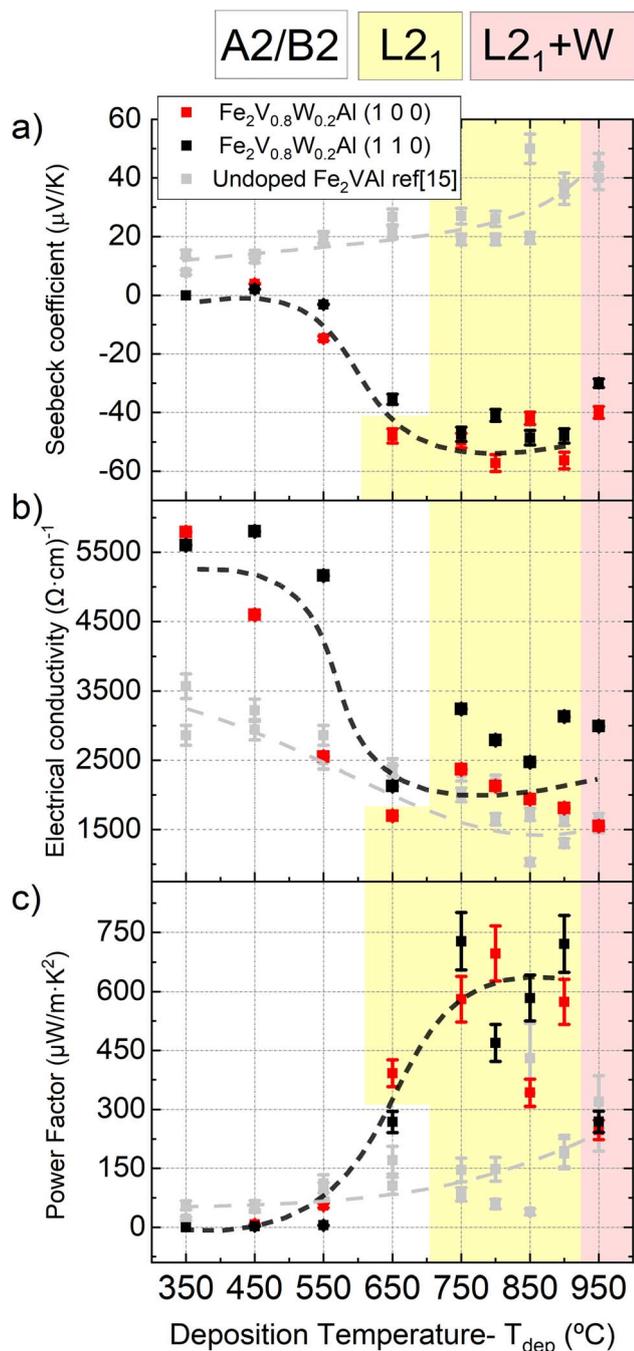
This journal is © The Royal Society of Chemistry 2026

Fig. 2 Room temperature thermoelectric properties as a function of deposition temperature (T_{dep}) of (1 0 0) (red) and (1 1 0) (black) oriented $Fe_2V_{0.8}W_{0.2}Al$ thin films. (a) Seebeck coefficient (S), (b) electrical conductivity (σ) and (c) power factor (PF). Highlighted in yellow are regions corresponding to samples with $L2_1$ ordering, and in red those with $L2_1$ ordering and W crystallization. Along with these values, data from[15] is displayed for comparison (light grey).

corresponding values obtained on W-free Fe_2VAl films grown under identical conditions, as reported previously.[15] It is evident in Fig. 2a), that $Fe_2V_{0.8}W_{0.2}Al$ films show a negative Seebeck coefficient, confirming their expected n-type nature. Two clear regions are observed: one with lower Seebeck values (below -20 $\mu V\ K^{-1}$) for samples with A2–B2 phases (white background-

colored), and another one with higher Seebeck values, around -40 to -60 $\mu V\ K^{-1}$, for samples with the $L2_1$ phase (yellow background-colored). W segregation (red background-colored) gives rise to a blend of $L2_1$ and pure W, and is not directly comparable with the rest of non-W segregated samples, though its Seebeck value is also plotted. The maximum Seebeck coefficient of 57 ± 3 $\mu V\ K^{-1}$ was observed for the sample grown on MgO at 800 °C. This value represents substantial improvements over disordered phases.

The electrical conductivity, shown in Fig. 2b), presents two clear regions with higher (on average 5250 $(\Omega\ cm)^{-1}$) and reduced values (on average 2250 $(\Omega\ cm)^{-1}$), associated with both A2–B2 and $L2_1$ phases, respectively. Interestingly, (110) oriented films consistently present superior electrical conductivity compared to their (100) counterparts, attributed to different epitaxial relations, distinct morphological characteristics, and orientation-dependent crystallization mechanisms on the two different substrates. The competing effects of enhanced Seebeck coefficient and reduced electrical conductivity described above result in overall PF improvements for $L2_1$ ordered phases. As shown in Fig. 2c) maximum power factor values are 730 ± 70 $\mu W\ m^{-1}\ K^{-2}$, representing more than two-fold enhancement compared to A2–B2 phases. Also, some minor differences of Seebeck and conductivity values within the $L2_1$ regime can be observed, which are attributed to experimental scattering in sample properties, minor changes in chemical order and morphology and grain sizes variations (A summary table of differences of Seebeck coefficient, electrical conductivity and overall PF values between representative samples in the $L2_1$ regime and a B2 sample is shown in the SI). The drastic drop in PF for the samples grown at 950 °C directly correlate with detrimental effects of tungsten segregation. Fig. 2c) portrays the notable effect of $L2_1$ ordering in the PF, making more than a two-fold increase with respect to A2–B2 phases. When comparing these values of $Fe_2V_{0.8}W_{0.2}Al$ films with those obtained in undoped Fe_2VAl layers measured in our previous work,[15] clear differences arise. Tungsten incorporation produces several critical improvements over undoped Fe_2VAl films at room temperature and above: (1) carrier type switches from p-type to n-type with enhanced absolute Seebeck coefficients, (2) $L2_1$ phase's overall electrical conductivity increases from 1000–1600 $(\Omega\ cm)^{-1}$ in the undoped case to 1500–3250 $(\Omega\ cm)^{-1}$ in $Fe_2V_{0.8}W_{0.2}Al$ films, and (3) $L2_1$ phase's average power factor enhances from $\sim$150–450 $\mu W\ m^{-1}\ K^{-2}$ (undoped) to $\sim$350–750 $\mu W\ m^{-1}\ K^{-2}$ (tungsten-doped).

To understand the electronic transport characteristics of A2, B2 and $L2_1$-ordered films, the Hall coefficient at room temperature is presented in Fig. 3. Here, a positive Hall coefficient is observed for all samples, with a clear descending tendency with increasing T_{dep}. Remarkably, all samples exhibit a positive Hall coefficient and a negative Seebeck coefficient. This is an unusual behavior, characteristic of bipolar conduction with asymmetric carrier mobilities in multi-band systems transport.[18,26,27] This fact provides crucial insights into the underlying electronic structure modifications induced by tungsten substitution.
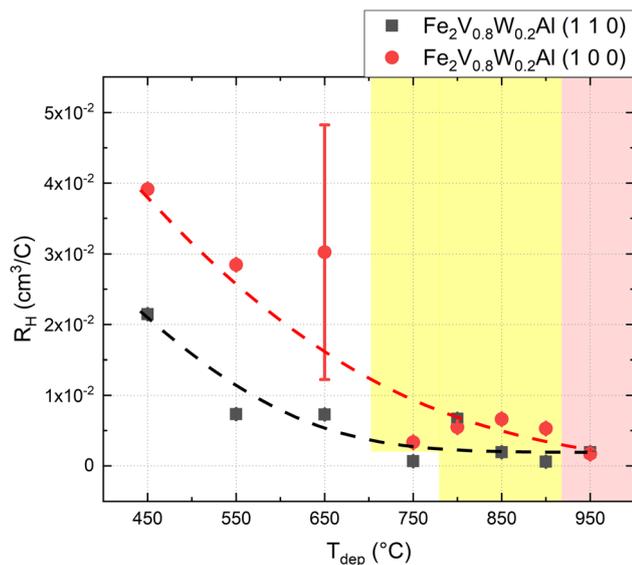
This journal is © The Royal Society of Chemistry 2026

J. Mater. Chem. A, 2026, 14, 12835–12845 | 12837

Fig. 3 Room temperature Hall coefficient as a function of deposition temperature (T_{dep}) of (100) (red) and (110) (black) oriented $Fe_2V_{0.8}$-$W_{0.2}Al$ thin films. Yellow and red highlighted regions correspond to samples with $L2_1$ ordering and $L2_1$ ordering with W crystallization, respectively.

Fig. 4 Unfolded band structure and DOS for $Fe_2V_{0.75}W_{0.25}Al$. Minority and majority spins are denoted with down and up arrows, respectively.

The negative Seebeck coefficient unambiguously confirms that electrons serve as the dominant charge carriers responsible for thermoelectric transport in the tungsten-doped system. However, the simultaneously positive Hall coefficient suggests that holes, despite constituting minority carriers, possess significantly higher mobility than electrons. This apparent contradiction is resolved through a detailed understanding of the fundamentally different weighting mechanisms governing each transport coefficient. The Seebeck coefficient is proportional to the conductivity-weighted energy derivative ($\propto \sigma_i \cdot \partial\mu_i/\partial E$), making it sensitive to carrier concentration and thus dominated by the high-density electron population. In contrast, the Hall coefficient is proportional to mobility-squared weighted averages ($\propto \Sigma\mu_i^2 \cdot n_i\, e_i$), making it sensitive to carrier mobility and potentially dominated by high-mobility holes even when they represent minority carriers.

This transport asymmetry likely originates from the complex band structure modifications induced by tungsten substitution within the highly ordered $L2_1$ Heusler phase. In Fig. 4 the unfolded band structure calculated from Density Functional Theory calculations is depicted along with the spin-resolved density of states (DOS). As the calculations reveal, carriers donated by the dopant are located in the conduction band, forming pockets with very different effective masses and mobilities. Specifically, some bands below the Fermi energy in the conduction band exhibit flat dispersion, indicating heavy effective masses and low mobilities, which can significantly impede electronic transport. Using DFT band structure calculations depicted in Fig. 4 and supposing a temperature of 300 K, the estimated carrier concentrations of electrons and holes are $n_e \sim 5 \times 10^{21}$ cm^{-3} and $n_h \sim 2 \times 10^{18}$ cm^{-3}, respectively, yielding a ratio of carrier concentrations of three orders of magnitude. Using these concentrations, and the estimated effective masses
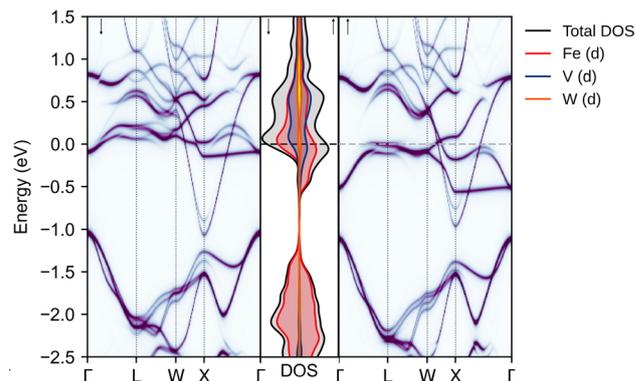
of m_{eff} (e−)$\sim$1.3–2.3$\cdot m_e$ and m_{eff}(h$^+$)$\sim$0.8–1.3$\cdot m_e$, obtained through parabolic band approximations, Books-Herring model yields a mobility ratio of holes and electrons of $\mu_h/\mu_e \sim$100–1000. Assuming $\mu_h/\mu_e = 100$ and carrier concentrations of $n_e = 5 \times 10^{21}$ cm^{-3} and $n_h = 2 \times 10^{18}$ cm^{-3}, the ambipolar Hall coefficient $R_h = (n_h \times \mu_h^2 − n_e \times \mu_e^2/(e\,(n_h \times \mu_h + n_e \times \mu_e)^2))$ results in $R_h = 3\ 10^{-3}$, which aligns with the measured values on $L2_1$-ordered films shown in Fig. 3. Simultaneously, these flat bands are expected to produce a large density of states, consequently yielding a higher Seebeck coefficient.

While bipolar effects have traditionally been associated with a reduction in thermoelectric performance and thus considered something to be avoided, the asymmetric bipolar conduction mechanism has been also postulated for other materials systems such as $LaCoO_3$,[28] BiSb,[29] GaN[30] and it has been suggested as a strategy to improve performance in thermoelectric materials.[31] Based on the DOS, W-doped Fe_2VAl should exhibit a significantly larger Seebeck coefficient than its undoped counterpart. However, the absolute values experimentally obtained are in the same order of magnitude, which is likely attributable to the reduction in the Seebeck coefficient in the W-doped material due to bipolar effects. Meanwhile, electrical conductivity is expected to increase due to the contribution of these light holes.

Fig. 5 presents temperature-dependent thermoelectric properties for representative films with and without chemical ordering. Seebeck coefficients show minimal temperature dependence while maintaining the remarkable ordering-induced enhancements already observed at room temperature. Electrical conductivity increases with temperature for all samples. This can be explained taking into account the bipolar nature of the samples, as this nature becomes more pronounced with increasing temperature due to thermal activation of minority carriers across the narrow band gap. This temperature evolution of the transport coefficients provides additional validation of the proposed multi-band conduction mechanism and demonstrates the sophisticated electronic engineering achieved through strategic tungsten substitution in the Fe_2VAl Heusler matrix. This bipolar transport mechanism with asymmetric carrier properties actually represents advantageous physics for thermoelectric applications. The system
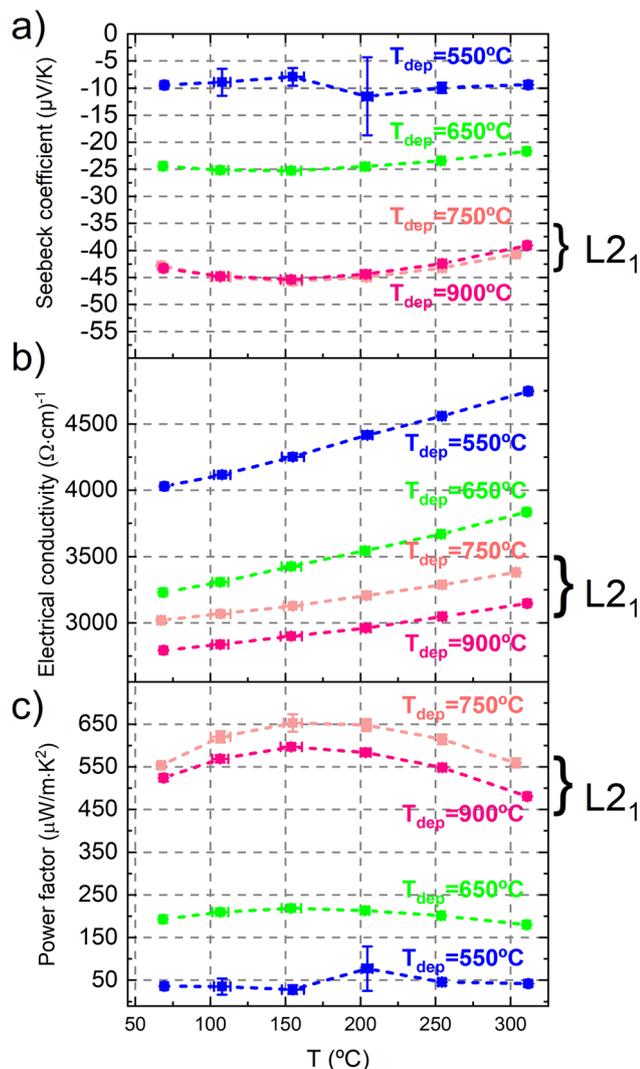
12838 | J. Mater. Chem. A, 2026, 14, 12835–12845

This journal is © The Royal Society of Chemistry 2026

Fig. 5 Temperature dependence of (a) Seebeck coefficient (S), (b) electrical conductivity (σ), and power factor (PF) of representative films with different degrees of chemical order. At the right of (a–c), an arrow is depicted indicating the plots corresponding to films with $L2_1$ ordering.

maintains high electrical conductivity through the combined contribution of both carrier types while preserving substantial Seebeck coefficients through the dominance of electron transport in the thermoelectric response. The resulting temperature-dependent power factor evolution demonstrates consistently superior performance for $L2_1$ ordered samples across all measured temperatures, with peak values reaching 650 ± 20 μW m^{-1} K^{-2} at 150 °C for the film deposited $T_{dep} = 750$ °C on Al$_2$O$_3$. The $L2_1$ ordered Fe$_2$V$_{0.8}$W$_{0.2}$Al film reach power factors of almost 3 times higher than its B2 phase counterparts.

Fig. 6 presents comprehensive thermoelectric performance comparison between tungsten-doped Fe$_2$V$_{0.8}$W$_{0.2}$Al $L2_1$-ordered and undoped Fe$_2$VAl $L2_1$-ordered films (both grown at $T_{dep} = 900$ °C), including power factor, thermal conductivity, and figure of merit evolution with temperature.

In the case of the power factor (Fig. 6a)), when comparing W-doped (Fe$_2$V$_{0.8}$W$_{0.2}$Al) and undoped (Fe$_2$VAl) with the $L2_1$-ordered films, both grown at 900 °C. They present a maximum power factor of 600 μW m^{-1} K^{-2} and 480 μW m^{-1} K^{-2} for doped and undoped cases at the temperatures of 150 °C and 105 °C, respectively. It is worth noting that at 300 °C, the difference in PFs between undoped and W-doped samples is even more pronounced, exceeding a factor of two.

Simultaneously, the tungsten substitution also results in a reduction of thermal conductivity at room temperature from 4.6 W m^{-1} K^{-1} to 1.4 W m^{-1} K^{-1} (Fig. 6b)), for the W-substituted case. Moreover, at 105 °C, which corresponds to the maximum in the power factor, the thermal conductivity of the undoped sample is 6.9 ± 0.5 W m^{-1} K^{-1}, compared to 2.0 ± 0.4 W m^{-1} K^{-1} for the W-doped sample. At the maximum measured temperature of 300 °C, the undoped and W-doped samples
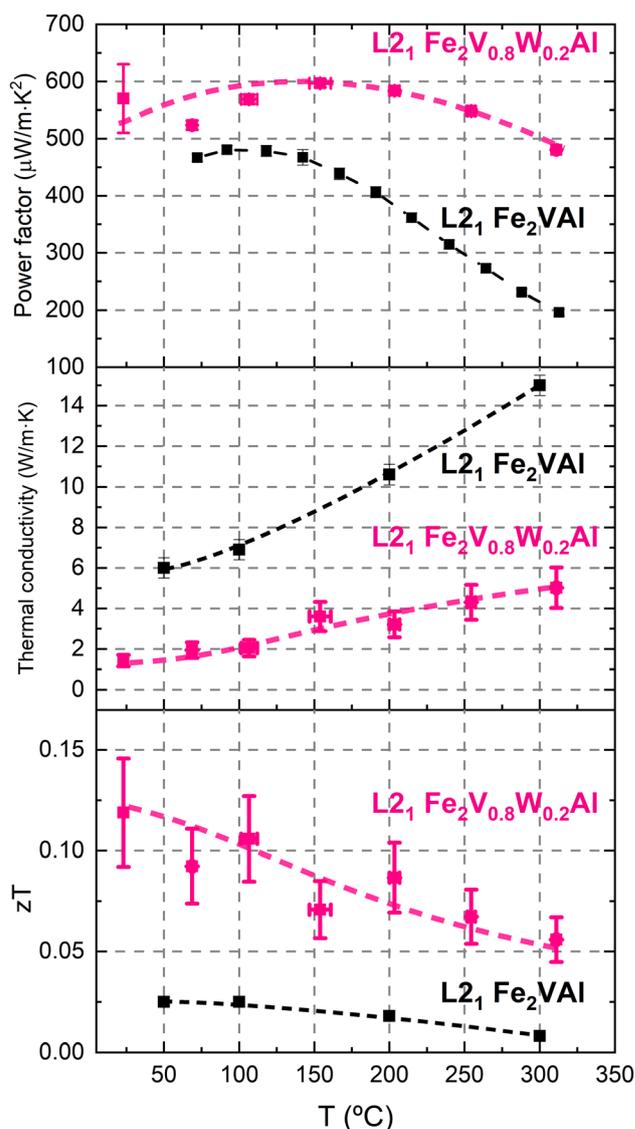

Fig. 6 Temperature dependence of (a) power factor (PF), (b) thermal conductivity (κ), and (c) zT of a representative $L2_1$-ordered film deposited at 900 °C on Al$_2$O$_3$ and $L2_1$ Fe$_2$VAl from our previous work.[15]

This journal is © The Royal Society of Chemistry 2026

J. Mater. Chem. A, 2026, **14**, 12835–12845 | **12839**

show thermal conductivities of 15 ± 0.5 W m^{-1} K^{-1} and 5 ± 1 W m^{-1} K^{-1}, respectively. This reduction in thermal conductivity in entire measured temperature range can be explained because adding a heavy atom like W enhances the scattering of phonons. While the increase in thermal conductivity with temperature demonstrates that the electronic contribution plays a key role in both W-doped and undoped Fe_2VAl, the reduction of κ upon doping stems from a significant decrease in the lattice contribution.
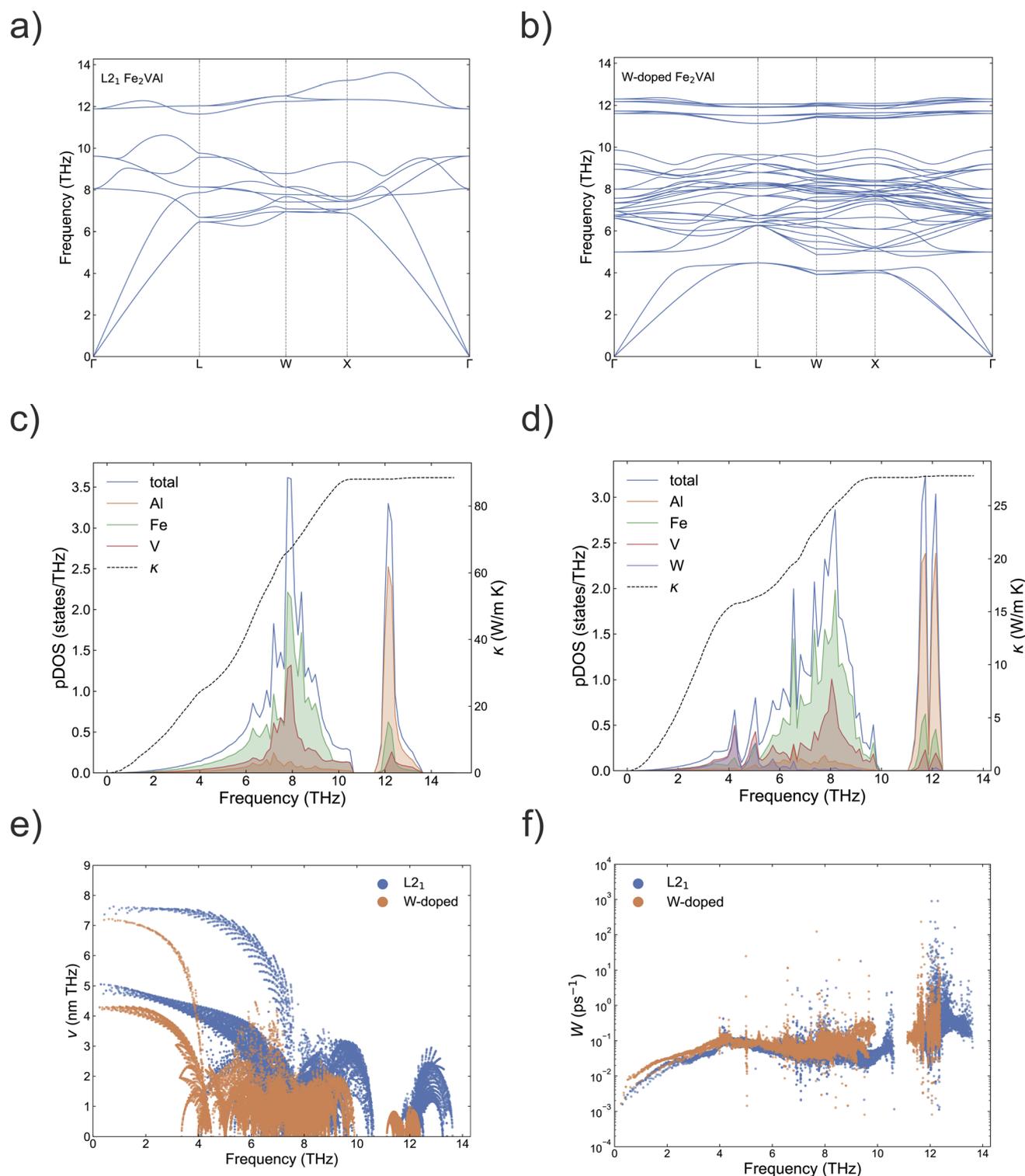

Fig. 7 (a and b) Phonon dispersion curves, (c and d) vibrational density of states and cumulative lattice thermal conductivity, (e) group velocities, and (f) scattering rates for undoped and W-doped L2$_1$ Fe$_2$VAl models at 300 K.

12840 | J. Mater. Chem. A, 2026, 14, 12835–12845

This journal is © The Royal Society of Chemistry 2026

Notably, B2 and L2$_1$ Fe$_2$V$_{0.8}$W$_{0.2}$Al films exhibit similar thermal conductivity values at room temperature (1.5 ± 0.3 W m^{-1} K^{-1} and 1.4 ± 0.3 W m^{-1} K^{-1} respectively). This indicates that the incorporation of W is the main responsible for the reduction of thermal conductivity as it affects the phononic structure, which is not related to the band structure modifications made by L2$_1$ ordering.

The synergistic combination of enhanced power factors due to the improved chemical order and reduced thermal conductivities due to the substitution of V for a heavier element yields remarkable zT improvements approaching one order of magnitude enhancement over undoped systems. Fig. 6c) shows that maximum zT values reach 0.12 ± 0.03 at room temperature and 0.105 ± 0.020 at 150 °C, representing competitive performance with state-of-the-art thermoelectric materials. The aforementioned multi-carrier optimization mechanism, combined with the dramatic reduction in thermal conductivity achieved through enhanced phonon scattering, underlies the exceptional thermoelectric performance enhancement in the tungsten-doped Heusler films.

W-doping has a multifaceted effect on thermal transport. To further understand this effect, a comparison of the calculated dispersion curves, the phonon density of states, the group velocities, and the scattering rates for L2$_1$ Fe$_2$VAl and Fe$_2$V$_{0.8}$W$_{0.2}$Al is depicted in Fig. 7. From Fig. 7a–d it is observed that the vibrational modes associated with W atoms are located just above the acoustic modes, which drastically reduces their group velocities, which are presented in Fig. 7e). Additionally, scattering rates, plotted in Fig. 7f), are increased due to the larger number of scattering processes and the enhanced anharmonicity of the system. Cumulative lattice thermal conductivity, computed as a function of the frequency contributions of each vibrational mode plotted in Fig. 7c and d, shows that the acoustic modes' contribution is strongly reduced when W is included. For instance, at 4 THz, the cumulative thermal conductivity of the doped system has been reduced by half with respect to the undoped system. Additionally, when considering the average grain size of the samples, a lattice thermal conductivity of 6.44 W m^{-1} K^{-1} is obtained for the doped L2$_1$ samples with an average grain size of 20 nm (see figure SI 10 of the SI). However, although W has been explicitly included in the conventional cell, this model cannot account for the long-range effects of W atoms randomly distributed in the lattice. As an approximation, and similarly to the approach we followed for modeling the anisotropic effect in our previous work, we have incorporated the Tamura model[32] to account for the mass disorder effect of randomly distributed W atoms in the lattice. Using this approach, we obtained a lattice thermal conductivity of 1.01 W m^{-1} K^{-1} for average grain sizes around 20 nm at 300 K. In summary, the extremely low thermal conductivities of the samples arise from three contributions. Dopant-induced local distortions enhance scattering rates and reduce group velocities, thereby lowering the lattice thermal conductivity of single-crystal samples to 27.8 W m^{-1} K^{-1}. Accounting for dopant/mass disorder further reduces lattice thermal conductivity to 5.79 W m^{-1} K^{-1}, and finally, considering the grain size of thin films

yields 1.01 W m^{-1} K^{-1}, which is very close to the experimental values.

Comparative analysis with literature reveals interesting composition-performance relationships. While Machda et al. and Mikami et al.[17,25] achieved higher power factors (1600 and ~2600 μW m^{-1} K^{-2}, respectively) than the maximum values reported in this work (730 ± 70 μW m^{-1} K^{-2}) with lower tungsten concentrations (Fe$_2$V$_{0.9}$W$_{0.1}$Al), they observed correspondingly higher thermal conductivities (3.5 and 5 W m^{-1} K^{-1}, respectively compared with our value of 1.4 ± 0.3 W m^{-1} K^{-1}). The highest figure of merit, zT = 0.12 ± 0.03, in the films grew in this study is obtained at room temperature and it is similar to the ones obtained by the two mentioned works (0.16 at 70–150 °C by Machda et al.,[17] 0.2 at 120 °C by Mikami et al.[25]). This suggests that a complementary behavior of thermoelectric properties exists, where higher doping levels sacrifice power factor for thermal conductivity benefits.

Comparison with silicon-doped systems (Hiroi et al.[33] and Lue et al.[22]) reveals complementary advantages for heavy element doping. While silicon-doped systems achieve exceptionally high-power factors (2200–2900 μW m^{-1} K^{-2}), their elevated thermal conductivities (12.6–19 W m^{-1} K^{-1}) result in inferior zT values (0.036–0.06), confirming the strategic advantage of heavy atom substitution for overall thermoelectric performance optimization.

To further understand the behavior of this material and the effect of doping on its electrical properties, it is necessary to know how its band structure changes when W doping is present. For this reason, it is highly interesting to evaluate the band gap of this material and compare the magnitude with the one obtained on undoped Fe$_2$VAl. To accomplish this, optical methods were employed, as it is seen in Fig. 8, where a Tauc plot analysis[34] of indirect transitions in Fe$_2$V$_{0.8}$W$_{0.2}$Al reveals a bandgap value of 0.23 ± 0.01 eV for L2$_1$ ordered films, closely matching previously measured undoped Fe$_2$VAl values (0.19 ± 0.05 eV). DFT calculation seems in good agreement with
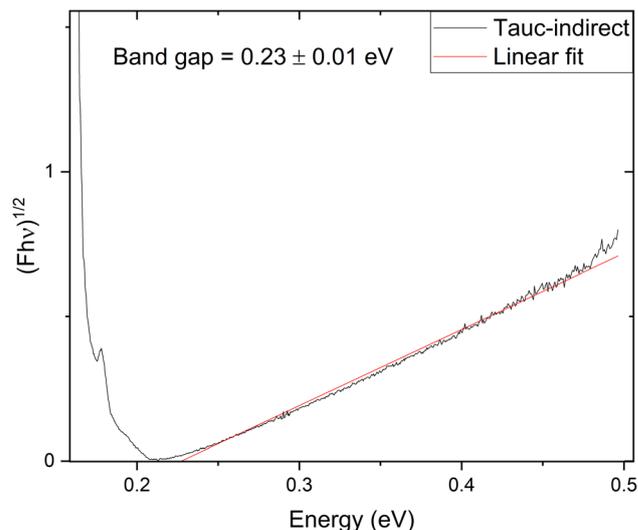
Fig. 8 Tauc plot used for the estimation of the indirect band gap (E_g = 0.23 ± 0.01 eV) of Fe$_2$V$_{0.8}$W$_{0.2}$Al deposited at 850 °C on Al$_2$O$_3$.

This journal is © The Royal Society of Chemistry 2026

J. Mater. Chem. A, 2026, **14**, 12835–12845 | **12841**

experimental measurements, obtaining an energy difference for the majority spin between the valence and conduction band of 0.16 eV. This similarity suggests that while tungsten incorporation produces significant electronic structure modifications, the fundamental band gap remains relatively unchanged. DFT calculations indicate a rigid upward band shift of approximately $\sim$1 eV upon W incorporation, consistent with the observed n-type behavior.

Conclusions

This comprehensive investigation demonstrates that $L2_1$ chemical ordering synergistically enhances the thermoelectric performance of tungsten-substituted Fe_2VAl thin films through complementary electronic and phononic mechanisms. Tungsten incorporation successfully transforms Fe_2VAl from p-type to n-type semiconducting behavior. Furthermore, it simultaneously improves the power factor and dramatically reduces the thermal conductivity.

The systematic control of chemical ordering through deposition temperature optimization reveals that Seebeck coefficient enhancements observed in undoped $L2_1$ Fe_2VAl extend to tungsten-doped systems. Moreover, the reduction in electrical conductivity is overcompensated by Seebeck improvements, yielding overall power factor gains. Thin film synthesis provides inherent thermal conductivity benefits, while tungsten substitution delivers additional two-fold thermal conductivity reductions, culminating in $zT = 0.12 \pm 0.03$ at room temperature.

Compared to undoped Fe_2VAl, tungsten-doped alloys demonstrate more than a four-fold thermoelectric figure of merit improvement, establishing the critical importance of $L2_1$ chemical ordering for practical thermoelectric applications. While Machda et al.[17] achieved higher power factors (PF = 1600 μW m^{-1} K^{-2}) at lower W content ($W_{0.1}$), they reported correspondingly higher thermal conductivity ($\kappa = 3.5$ W m^{-1} K^{-1}). Our $W_{0.2}$ composition presents a complementary trade-off: sacrificing PF for dramatic κ reduction, yielding comparable zT values. This work thus demonstrates that chemical ordering control can partially compensate for non-optimal composition selection, a finding valuable for practical materials engineering. The successful implementation of industrially scalable magnetron sputtering for high-performance thin film synthesis enables promising pathways for commercial thermoelectric device fabrication.

This work ultimately validates the viability of doped Fe_2VAl-based full Heusler alloys as sustainable, non-toxic, and earth-abundant thermoelectric materials for near-room temperature applications. Thus, making this family of material suitable for waste heat recovery systems, IOT, and wearable devices contributing to global sustainable energy solutions, and addressing critical challenges in the ongoing energy transition.

Experimental details

A series of 150 nm $Fe_2V_{0.8}W_{0.2}Al$ films was simultaneously deposited on MgO (1 0 0) and Al_2O_3 ($11\bar{2}0$) substrates at temperatures (T_{dep}) ranging from 350 °C to 950 °C. The

deposition was carried out in a UHV chamber (base pressure $\sim$10^{-9} mbar) utilizing DC magnetron sputtering. A stoichiometric commercial $Fe_2V_{0.8}W_{0.2}Al$ target (Mateck GmbH) was sputtered at 40 W and 2.5 10^{-3} mbar Ar pressure, yielding a deposition rate of 1.67 nm min^{-1}. T_{dep} was measured in situ using a calibrated thermocouple located in the sample holder.

The crystal structure was characterized by X-ray Diffraction (XRD) measurements performed on a Bruker D8 Discover four-circle diffractometer with a microfocus X-ray source (IμS) (Cu Kα_1) and an Eiger2 2D detector. Electrical conductivity and charge carrier concentration at RT were measured using a four-probe commercial HMS 5500 Hall effect measurement system (Ecopia). RT Seebeck measurements were performed utilizing a lab-made system in the in-plane direction. Temperature-dependent Seebeck coefficient and electrical conductivity measurements were carried out using a two-probe commercial Linseis LSR-3 system.

The thermal conductivity was measured in the out-of-plane direction using the time-domain thermo-reflectance (TDTR) method at various temperatures, utilizing the Front/Front configuration. The measurements were performed with a PicoTR system (PicoTherm), employing pump and probe lasers with wavelengths of 1550 nm and 750 nm, respectively. Both lasers feature a pulse duration of 0.5 ps, and the laser pulses were applied to the film (after depositing a thin Pt layer of 100 nm on top of it) within a time interval of 50 ns. From these measurements, the thermal diffusivity is obtained. Knowing the parameters of density and heat capacity of the film and substrate the thermal conductivity was calculated. Parameters used for the film were density of 7.05 $\pm$ 0.1 g cm^{-3}, estimated through X-ray reflectometry, and heat capacity of 455.89 J kg^{-1} K^{-1}, estimated from the Themtest Instrument Co. bulk materials database.[35]

Morphological characterization was carried out via a FEI Verios 460, Scanning Electron Microscope (SEM). The band gap was determined from mid-IR optical reflectance measurements (from 2.5 to 17 μm) using a PerkinElmer (Spectrum 3) Fourier Transform Infrared (FT-IR) spectrophotometer, analyzed with the Tauc approaches.[34]

Computational details

Ground states were fully relaxed (atoms and lattice) using the VASP package[36] and projector-augmented wave potentials.[37] Energies and wave functions were computed using the meta-GGA r^{2}SCAN functional proposed by Furness et al.[38] This functional provides a good balance between computational efficiency and accuracy for band gap predictions, mitigating the underestimation typical of GGA functionals while achieving a mean absolute error comparable to that of hybrid exchange-correlation functionals.[39–41] Moreover, as reported in our previous study, r^{2}SCAN reproduces the experimental narrow-band-gap semiconductor behavior of Fe_2VAl.[15] Core and valence electrons were selected following the standards proposed by Calderon et al.[42] A kinetic energy cutoff of 500 eV was applied to the plane-wave basis set expansion to mitigate Pulay stress errors. A dense mesh of 8000 k-points per reciprocal

12842 | J. Mater. Chem. A, 2026, 14, 12835–12845

This journal is © The Royal Society of Chemistry 2026

atom was used to accurately describe the minimum of the potential energy surface and the ground state wavefunction.

Geometry and lattice vectors were subjected to full relaxation until the forces on each atom were below 10^{-7} eV Å^{-1}. Wavefunction convergence was achieved when the energy difference between successive electronic steps fell below 10^{-9} eV, incorporating an additional support grid for the evaluation of augmentation charges to minimize force-related noise. W-doped model was obtained by substituting a V atom with W in a conventional 16-atom cell, achieving a doping level close to the experimental values and within the range of experimental error. To compare the electronic structure of the L2$_1$ phase and doped structure, band structure unfolding[43] was performed using the easyunfold code.[44]

Lattice thermal conductivity was calculated by combining the hiPhive[45] and ShengBTE[46] packages using the hiPhive wrapper.[47] The force constants were obtained using 432-atom 3 × 3 × 3 supercells, using the conventional cell as unit cell. Interatomic force constants were calculated using a two-step process. Initially, 4 supercells underwent minor random atomic distortions. Subsequently, the hiPhive wrapper was used to extract second- and third-order IFCs. Following this, an additional 14 distorted supercells were generated by superimposing normal modes with random phase factors and amplitudes corresponding to a temperature of 300 K by employing the second-order IFCs obtained from the previous step. The interatomic force constants were obtained using the recursive feature elimination (RFE) algorithm, through multilinear regression to the DFT forces. Although this approach is more computationally demanding compared to ordinary least-squares regression, RFE has demonstrated higher efficacy in achieving convergence with a reduced number of structures. The effects of point defects on lattice thermal conductivity can be modeled using different approaches. On one hand, the Green's function approach—in which phonons of the perfect cell interact locally with the defect—provides a microscopic description of the scattering mechanisms, capturing the influence of substitutional disorder. This method has been previously used for pristine and substituted Fe$_2$VAl.[48] On the other hand, we opted to assume that defects modify all lattice phonons and thus the harmonic and anharmonic interatomic force constants. This required explicit inclusion of the dopant during IFC calculations, which breaks the cell symmetry, increases the number of inequivalent IFCs, and raises the computational cost. While this method is extremely expensive when interatomic force constants are computed using single-atom finite displacements, multilinear regression approaches for extracting IFCs reduce the computational cost and open the door to consider the local geometry distortions that dopants induce in the material's vibrational properties—particularly when dopants are considerably large ions such as W. Despite W doping being explicitly included in the atomistic model, this does not capture the long-range disorder of the dopants. To assess the impact of such long-range disorder on the thermoelectric properties, the Tamura model,[32] including an isotopic or elastic scattering term that accounts for mass disorder. This approach was successfully used previously to model the effect of

antisite disorder on the thermal conductivity of Fe$_2$VAl. The influence of grain size on lattice thermal conductivity was considered by determining the cumulative thermal conductivities based on phonon mean free paths; the value of κ_1 for a specific particle size L is estimated by summing the contributions from all mean free paths up to L. To balance memory demand and ensure the convergence of κ_1 with respect to q-points, a Gaussian smearing of 0.1 is applied along with a dense mesh of 30 × 30 × 30 q-points.

Conflicts of interest

There are no conflicts to declare.

Data availability

All the data supporting the findings will be available at https://digital.csic.es/ after publication. Additional data are available from the corresponding author upon reasonable request.

Supplementary information (SI) is available. See DOI: https://doi.org/10.1039/d5ta09938b.

Acknowledgements

References

1 M. Martin-Gonzalez, K. Lohani and N. Neophytou, Phonon and electron transport engineering for enhanced thermoelectric performance and the challenges of device integration, *Energy Mater.*, 2025, **5**, 500121, DOI: 10.20517/energymater.2025.32.

2 I. T. Witting, T. C. Chasapis, F. Ricci, M. Peters, N. A. Heinz, G. Hautier and G. J. Snyder, The Thermoelectric Properties of Bismuth Telluride, *Adv. Electron. Mater.*, 2019, **5**, 1800904, DOI: 10.1002/aelm.201800904.

3 P. Cervino-Solana, M. J. Ramirez-Peral, M. S. Martín-González and O. Caballero-Calero, Thermoelectric bismuth telluride nanostructures fabricated by electrodeposition within flexible templates, *Heliyon*, 2024, **10**(16), e36114, DOI: 10.1016/j.heliyon.2024.e36114.

This journal is © The Royal Society of Chemistry 2026

J. Mater. Chem. A, 2026, **14**, 12835–12845 | **12843**

4 J. P. Heremans, V. Jovovic, E. S. Toberer, A. Saramat, K. Kurosaki, A. Charoenphakdee, S. Yamanaka, G. J. Snyder, et al., Enhancement of Thermoelectric Efficiency in PbTe by Distortion of the Electronic Density of States, Science, 2008, 321(5888), 554–557, DOI: 10.1126/science.1159725.

5 J. A. Perez-Taborda, O. Caballero-Calero, L. Vera-Londono, F. Briones and M. Martin-Gonzalez, High Thermoelectric zT in n-Type Silver Selenide films at Room Temperature, Adv. Energy Mater., 2018, 8, 1702024, DOI: 10.1002/aenm.201702024.

6 Y. Liu, T. Kleinhanns, S. Horta, E. P. Dutkiewicz-Kopczynska, S. Lu, M. C. Spadaro, A. Genç, L. Chen, K. H. Lim, M. Hong, J. Arbiol and M. Ibañez, Liquid–Solid Interface Reactions Drive Enhanced Thermoelectric Performance in Ag$_2$Se, J. Am. Chem. Soc., 2025, 147(35), 32199–32208, DOI: 10.1021/jacs.5c11435.

7 C. V. Manzano, C. Llorente del Olmo, O. Caballero-Calero and M. Martín-González, High thermoelectric efficiency in electrodeposited silver selenide films: from Pourbaix diagram to a flexible thermoelectric module, Sustain. Energy Fuels, 2021, 5(18), 4597–4605, DOI: 10.1039/D1SE01061A.

8 C. Zhou, Y. K. Lee, Y. Yu, S. Byun, Z. Z. Luo, H. Lee, B. Ge, Y. L. Lee, X. Chen, J. Y. Lee, O. Cojocaru-Miréin, H. Chang, J. Im, S. P. Cho, M. Wuttig, V. P. Dravid, M. G. Kanatzidis and I. Chung, Polycrystalline SnSe with a thermoelectric figure of merit greater than the single crystal, Nat. Mater., 2021, 20(10), 1378–1384, DOI: 10.1038/s41563-021-01064-6.

9 C.-L. Chen, H. Wang, Y.-Y. Chen, T. Day and G. J. Snyder, Thermoelectric properties of p-type polycrystalline SnSe doped with Ag, J. Mater. Chem. A, 2014, 2(29), 11171–11176, DOI: 10.1039/C4TA01643B.

10 J. A. Perez-Taborda, L. Vera, O. Caballero-Calero, E. O. Lopez, J. J. Romero, D. G. Stroppa, F. Briones and M. Martin-Gonzalez, Pulsed Hybrid Reactive Magnetron Sputtering for High zT Cu$_2$Se Thermoelectric Films, Adv. Mater. Technol., 2017, 2, 1700012, DOI: 10.1002/admt.201700012.

11 H. Liu, X. Yuan, P. Lu, X. Shi, F. Xu, Y. He, Y. Tang, S. Bai, W. Zhang, L. Chen, Y. Lin, L. Shi, H. Lin, X. Gao, X. Zhang, H. Chi and C. Uher, Ultrahigh Thermoelectric Performance by Electron and Phonon Critical Scattering in Cu$_2$Se$_{1-x}$I$_x$, Adv. Mater., 2013, 25(45), 6607–6612, DOI: 10.1002/adma.201302660.

12 O. Caballero-Calero, J. R. Ares and M. Martín-González, Environmentally Friendly Thermoelectric Materials: High Performance from Inorganic Components with Low Toxicity and Abundance in the Earth, Adv. Sustain. Syst., 2021, 5, 2100095, DOI: 10.1002/adsu.202100095.

13 F. Garmroudi, M. Parzer, A. Riss, A. V. Ruban, S. Khmelevskyi, M. Reticcioli, M. Knopf, H. Michor, A. Pustogow, T. Mori and E. Bauer, Anderson transition in stoichiometric Fe$_2$VAl: high thermoelectric performance from impurity bands, Nat. Commun., 2022, 13, 3599, DOI: 10.1038/s41467-022-31159-w.

14 H. Miyazaki, S. Kimura, K. Onishi, T. Hihara, M. Yoshimura, H. Ishii, M. Mikami and Y. Nishino, Relation between Electronic Structure and Thermoelectric Properties of Heusler-Type Ru2VAl Compounds, Crystals, 2022, 12, 1403, DOI: 10.3390/cryst12101403.

15 J. M. Domínguez-Vázquez, O. Caballero-Calero, K. Lohani, J. J. Plata, A. M. Marquez, C. V. Manzano, M. A. Tenaguillo, H. Ohta, A. Cebollada, A. Conca and M. Martín-González, Thermoelectric performance boost by chemical order in epitaxial L21 (100) and (110) oriented undoped Fe2VAl thin films: an experimental and theoretical study, J. Mater. Chem. A, 2025, 13(30), 24716–24726, DOI: 10.1039/D5TA02619A.

16 M. Parzer, A. Kositz, J. Süß, F. Garmroudi, T. Mori and E. Bauer, Enhanced thermopower by double-site substitution of Ti in Fe2(VAl)1-xTi2x, Mater. Today Phys., 2025, 54, 101712, DOI: 10.1016/J.MTPHYS.2025.101712.

17 F. Machda, S. Singh, K. Kuga, A. K. R. Ang, M. Matsunami and T. Takeuchi, Thermoelectric performance of Fe2V0.9W0.1Al thin films deposited on n-type Si substrates, Jpn. J. Appl. Phys., 2023, 62, 055502, DOI: 10.35848/1347-4065/accfd7.

18 B. Hinterleitner, I. Knapp, M. Poneder, Y. Shi, H. Müller, G. Eguchi, C. Eisenmenger-Sittner, M. Stöger-Pollach, Y. Kakefuda, N. Kawamoto, Q. Guo, T. Baba, T. Mori, S. Ullah, X. Chen and E. Bauer, Thermoelectric performance of a metastable thin-film Heusler alloy, Nature, 2019, 576(7785), 85–90, DOI: 10.1038/s41586-019-1751-9.

19 M. Mikami, T. Kamiya and K. Kobayashi, Microstructure and thermoelectric properties of Heusler Fe2VAl thin-films, Thin Solid Films, 2010, 518(10), 2796–2800, DOI: 10.1016/J.TSF.2009.08.029.

20 F. Garmroudi, A. Riss, M. Parzer, N. Reumann, H. Müller, E. Bauer, S. Khmelevskyi, R. Podloucky, T. Mori, K. Tobita, Y. Katsura and K. Kimura, Boosting the thermoelectric performance of Fe2VAl–type Heusler compounds by band engineering, Phys. Rev. B, 2021, 103(8), 085202, DOI: 10.1103/PhysRevB.103.085202.

21 N. Claus, S. Pairis, O. Leynaud and D. Bourgault, Exploring Fe-V-Ta-Al Heusler thin films: thermoelectric properties and Anomalous Hall effect for spintronics applications, J. Magn. Magn. Mater., 2025, 633, 173554, DOI: 10.1016/j.jmmm.2025.173554.

22 C. S. Lue, C. F. Chen, J. Y. Lin, Y. T. Yu and Y. K. Kuo, Thermoelectric properties of quaternary Heusler alloys Fe2VAl1-x Six, Phys. Rev. B:Condens. Matter Mater. Phys., 2007, 75, 064204, DOI: 10.1103/PhysRevB.75.064204.

23 F. Garmroudi, M. Parzer, A. Riss, S. Beyer, S. Khmelevskyi, T. Mori, M. Reticcioli and E. Bauer, Large thermoelectric power factors by opening the band gap in semimetallic Heusler alloys, Mater. Today Phys., 2022, 27, 100742, DOI: 10.1016/j.mtphys.2022.100742.

24 Y. Terazawa, M. Mikami, T. Itoh and T. Takeuchi, Effects of Heavy Element Substitution on Electronic Structure and Lattice Thermal Conductivity of Fe2VAl Thermoelectric Material, J. Electron. Mater., 2012, 41(6), 1348–1353, DOI: 10.1007/s11664-011-1862-z.

25 M. Mikami, Y. Kinemuchi, K. Ozaki, Y. Terazawa and T. Takeuchi, Thermoelectric properties of tungsten-substituted Heusler Fe2VAl alloy, *J. Appl. Phys.*, 2012, **111**, 093710, DOI: 10.1063/1.4710990.

26 G. Eguchi and S. Paschen, Robust scheme for magnetotransport analysis in topological insulators, *Phys. Rev. B*, 2019, **99**(16), 165128, DOI: 10.1103/PhysRevB.99.165128.

27 C.-Z. Li, J.-G. Li, L.-X. Wang, L. Zhang, J.-M. Zhang, D. Yu and Z.-M. Liao, Two-Carrier Transport Induced Hall Anomaly and Large Tunable Magnetoresistance in Dirac Semimetal Cd3As2 Nanoplates, *ACS Nano*, 2016, **10**(6), 6020–6028, DOI: 10.1021/acsnano.6b01568.

28 R. Okazaki and K. Tomiyasu, Prominent electron-hole asymmetry in thermoelectric transport of LaCoO3, *Phys. Rev. B*, 2022, **105**(3), 035154, DOI: 10.1103/PhysRevB.105.035154.

29 R. Orenstein, K. Ciesielski, K. Synoradzki, J. Qu, F. A. Bipasha, L. C. Gomes, J. M. Adamczyk, S. Berger, E. Ertekin and E. S. Toberer, Complex thermoelectric transport in Bi-Sb alloys, *Appl. Phys. Rev.*, 2025, **12**(1), DOI: 10.1063/5.0237802.

30 J. E. Dill, C. F. C. Chang, D. Jena and H. G. Xing, Two-carrier model-fitting of Hall effect in semiconductors with dual-band occupation: A case study in GaN two-dimensional hole gas, *J. Appl. Phys.*, 2025, **137**, 025702, DOI: 10.1063/5.0248998.

31 P. Graziosi, Z. Li and N. Neophytou, Bipolar conduction asymmetries lead to ultra-high thermoelectric power factor, *Appl. Phys. Lett.*, 2022, **120**, 072102, DOI: 10.1063/5.0076967.

32 S. Tamura, Isotope scattering of dispersive phonons in Ge, *Phys. Rev. B:Condens. Matter Mater. Phys.*, 1983, **27**(2), 858–866, DOI: 10.1103/PhysRevB.27.858.

33 S. Hiroi, M. Mikami and T. Takeuchi, Thermoelectric properties of Fe2VAl-based thin-films deposited at high temperature, *Mater. Trans.*, 2016, **57**(9), 1628–1632, DOI: 10.2320/matertrans.E-M2016824.

34 J. Tauc, R. Grigorovici and A. Vancu, Optical Properties and Electronic Structure of Amorphous Germanium, *Phys. Status Solidi B*, 1966, **15**(2), 627–637, DOI: 10.1002/pssb.19660150224.

35 *Rule of Mixtures Calculator for Heat Capacity*. Accessed: Aug. 13, 2025. [Online]. Available: https://thermtest.com/thermal-resources/rule-of-mixtures.

36 G. Kresse and J. Hafner, Ab initio molecular dynamics for liquid metals, *Phys. Rev. B:Condens. Matter Mater. Phys.*, 1993, **47**(1), 558–561, DOI: 10.1103/PhysRevB.47.558.

37 P. E. Blöchl, Projector augmented-wave method, *Phys. Rev. B:Condens. Matter Mater. Phys.*, 1994, **50**(24), 17953–17979, DOI: 10.1103/PhysRevB.50.17953.

38 J. W. Furness, A. D. Kaplan, J. Ning, J. P. Perdew and J. Sun, Accurate and Numerically Efficient r2SCAN Meta-Generalized Gradient Approximation, *J. Phys. Chem. Lett.*, 2020, **11**(19), 8208–8215, DOI: 10.1021/acs.jpclett.0c02405.

39 P. Borlido, T. Aull, A. W. Huran, F. Tran, M. A. L. Marques and S. Botti, Large-Scale Benchmark of Exchange–Correlation Functionals for the Determination of Electronic Band Gaps of Solids, *J. Chem. Theory Comput.*, 2019, **15**(9), 5069–5079, DOI: 10.1021/acs.jctc.9b00322.

40 R. Kingsbury, A. S. Gupta, C. J. Bartel, J. M. Munro, S. Dwaraknath, M. Horton and K. A. Persson, Performance comparison of *r*2 SCAN and SCAN metaGGA density functionals for solid materials via an automated, high-throughput computational workflow, *Phys. Rev. Mater.*, 2022, **6**(1), 013801, DOI: 10.1103/PhysRevMaterials.6.013801.

41 M. Kothakonda, A. D. Kaplan, E. B. Isaacs, C. J. Bartel, J. W. Furness, J. Ning, C. Wolverton, J. P. Perdew and J. Sun, Testing the r^2 SCAN Density Functional for the Thermodynamic Stability of Solids with and without a van der Waals Correction, *ACS Mater. Au*, 2023, **3**(2), 102–111, DOI: 10.1021/acsmaterialsau.2c00059.

42 C. E. Calderon, J. J. Plata, C. Toher, C. Oses, O. Levy, M. Fornari, A. Natan, M. J. Mehl, G. Hart, M. B. Nardelli and S. Curtarolo, The AFLOW standard for high-throughput materials science calculations, *Comput. Mater. Sci.*, 2015, **108**, 233–238, DOI: 10.1016/J.COMMATSCI.2015.07.019.

43 V. Popescu and A. Zunger, Effective Band Structure of Random Alloys, *Phys. Rev. Lett.*, 2010, **104**(23), 236403, DOI: 10.1103/PhysRevLett.104.236403.

44 B. Zhu, S. R. Kavanagh and D. Scanlon, easyunfold: A Python package for unfolding electronic band structures, *J. Open Source Softw.*, 2024, **9**(93), 5974, DOI: 10.21105/joss.05974.

45 F. Eriksson, E. Fransson and P. Erhart, The Hiphive Package for the Extraction of High-Order Force Constants by Machine Learning, *Adv. Theory Simul.*, 2019, **2**, 1800184, DOI: 10.1002/adts.201800184.

46 W. Li, J. Carrete, N. A. Katcho and N. Mingo, ShengBTE: A solver of the Boltzmann transport equation for phonons, *Comput. Phys. Commun.*, 2014, **185**(6), 1747–1758, DOI: 10.1016/J.CPC.2014.02.015.

47 J. J. Plata, V. Posligua, A. M. Márquez, J. Fernandez Sanz and R. Grau-Crespo, Charting the Lattice Thermal Conductivities of I–III–VI 2 Chalcopyrite Semiconductors, *Chem. Mater.*, 2022, **34**(6), 2833–2841, DOI: 10.1021/acs.chemmater.2c00336.

48 M. S. T. Noutack, A. Diack-Rasselio, E. Alleno and P. Jund, Numerical and experimental determination of the thermal conductivity of pristine and substituted Fe2VAl, *J. Alloys Compd.*, 2021, **883**, 160828, DOI: 10.1016/j.jallcom.2021.160828.

This journal is © The Royal Society of Chemistry 2026

J. Mater. Chem. A, 2026, **14**, 12835–12845 | **12845**